Coalescence and migration of a droplet on a liquid pool with an inclined bottom wall

Pavan Kumar Kirar [1], Pankaj S. Kolhe [2], and Kirti Chandra Sahu [1,*]

[1] *Department of Chemical Engineering, Indian Institute of Technology Hyderabad, Sangareddy, 502 284, Telangana, India*

[2] *Department of Mechanical and Aerospace Engineering, Indian Institute of Technology Hyderabad, Sangareddy, 502 284, Telangana, India*

(Received 9 May 2022; accepted 25 August 2022; published 6 September 2022)

We experimentally investigate the curvature-driven migration and coalescence of an ethanol droplet on the free surface of an ethanol pool with an inclined bottom wall by employing a high-speed shadowgraph technique. Two distinct coalescence phenomena, migrating partial coalescence and multidrop pinch-off, in addition to the normal partial coalescence and complete coalescence are observed when the Weber number (We), liquid depth at the impact point (d_l/D), and inclination angle (θ) are varied. The three-phase contact line (TPCL) formed by the air-liquid interface on the inclined bottom wall and its curvature near the TPCL cause these unique dynamics. The coalescence behaviors are clearly demarcated by the regime maps drawn in d_l/D-We and θ-d_l/D spaces. We found that the transition between partial and complete coalescence occurs at We ≈ 10, regardless of liquid depth, and that, for $\theta = 18^\circ$, the influence of the inclined wall is apparent for We > 2, which increases as the inclination angle increases.

DOI: 10.1103/PhysRevFluids.7.094001

I. INTRODUCTION

The interaction of two interfaces is fascinating due to its intricate physics [1–7]. Coalescence of droplets on a liquid surface is ubiquitous in many practical applications, e.g., microfluidics, combustion, coatings, inkjet printing, soil erosion and air trapping on the sea surface [8–10], and natural phenomena, such as raindrops falling on a liquid surface [11–14]. Apart from the wide range of practical applications, this subject involves complex physics, such as the generation of capillary waves leading to the formation of satellite droplets pinching off from the free surface (known as partial coalescence phenomenon), crater formation (at low impact velocity), and splashing (at high impact velocity). Thus, several researchers have investigated the coalescence of droplets impacting in orthogonal [15–23] and oblique [24–28] directions in deep and shallow liquid pools.

In orthogonal impacts, when a low-velocity droplet touches the free surface, it floats until the air cushion between the droplet and the free surface of the liquid pool is pushed out. The droplet then coalesces and drains inside the pool, forming a neck at the point where it touches the free surface, which proliferates due to the strong capillary pressure around the contact region. This results in the creation of upward-moving vertically symmetrical capillary waves, which lead to the formation of a liquid column that is then necked near the contact region. The diameter of the neck reduces with time as a result of the inward pull exerted by surface tension, and a satellite drop pinches off [18,29]. This partial coalescence phenomenon is currently understood to be driven by the competition between gravity, viscosity, and interfacial tension forces, resulting in various regimes [15,16]. Apart from the

*ksahu@che.iith.ac.in

partial coalescence, other impacting outcomes, such as splashing, bouncing, and total coalescence, are also observed as the impact velocity of the droplet is varied [26,27,30–32].

When a droplet collides with a liquid surface at an angle to horizontal (oblique impacts), the liquid pool is subjected to two components of force due to this impact. As the angle of impingement increases, the vertical component of the force decreases while the horizontal component increases. As a result, the free surface deforms asymmetrically, and the upward-moving capillary waves are generated, resulting in asymmetrical crater formation. An oblique impact was found to surpass splashing and secondary droplet formation [24–26]. Leneweit *et al.* [28] found that when the Weber number, which signifies the relative importance of the inertia over the surface tension force, is large, there are no capillary waves, and instead, a lamella is ejected at the droplet front, which is partially made up of the droplet fluid. The balance of surface tension and inertial forces in the contact-line region determines whether this region of high curvature is warped by surface tension, creating capillary waves, or whether the impact's stagnation pressure presses out a lamella-shaped surface. The impact of a droplet falling vertically into a liquid pool with an inclined bottom wall is fundamentally different from oblique impacts. When a droplet collides with the shallow region of a liquid pool with an inclined bottom wall, it experiences a differential depth of liquid in the pool and curvature of the free surface formed near the three-phase contact line (TPCL) on the inclined wall, resulting in more distinct dynamics than observed in the orthogonal impacts in a deep liquid pool and oblique impacts. This is the focus of our research, which has not been studied yet to the best of our knowledge despite its importance in a variety of applications, such as oil spills, soil erosion, and forensic analysis [33,34]. Several researchers also investigated the collision dynamics of a droplet on moving liquid surfaces [27,35–37]. For instance, in this case of a droplet colliding with a moving free surface at an angle, Bird *et al.* [38] found asymmetrical azimuthal variation in the ejected rim during splashing, and only a part of the rim was found to participate in the satellite droplets formation. Castrejón-Pita *et al.* [36] observed splashing, bouncing, and surfing phenomena depending on the speed of moving film. Che *et al.* [27] studied the effects of the Ohnesorge and Reynolds numbers and reported bouncing, partial coalescence, complete coalescence, and splashing phenomena for a droplet impacting on a moving liquid film.

We experimentally investigate the coalescence dynamics of an ethanol droplet (of diameter, D) impacting vertically (with velocity, U) on an ethanol pool with an inclined bottom wall by employing a high-speed shadowgraph technique. The curvature of the free surface created by the inclined wall near TPCL significantly affects the coalescence dynamics and migration of the droplet on the free surface, in contrast to what happens when a droplet collides with a liquid surface at an angle. Furthermore, a parametric analysis is carried out to investigate the influence of the inclination angle of the bottom wall (θ), dimensionless shallow liquid depth (d_l/D) at the point of impingement, and the Weber number ($\mathrm{We} = \rho_l U^2 D/\sigma$) on droplet coalescence and its migration over the air-liquid interface of the liquid pool. Here ρ_l and σ are the density of ethanol and surface tension of the ethanol-air interface, respectively.

The rest of the paper is organized as follows. In Sec. II the details of the experimental setup and procedure used in our investigation are summarized. The results are presented and discussed in Sec. III, and the concluding remarks are given in Sec. IV.

II. EXPERIMENTAL SETUP AND PROCEDURE

Figure 1 depicts the experimental setup used in our study. It consists of (1) an acrylic container with an inclined bottom wall, (2) droplet generation and dispensing mechanism, and (3) a two-directional image acquisition system involving two high-speed cameras (Phantom VEO 640L) along with back-lit illumination systems and a computer to record the images. In accordance with previous research (e.g., [15,29,39]), we chose ethanol as the working fluid. The container is filled with ethanol such that it forms a three-phase contact line (TPCL) on the inclined bottom wall as shown in Fig. 1. We use a Cartesian coordinate system (x, y, z) with its origin coinciding with the TPCL. The droplet generation and dispensing system comprise a syringe pump (SP-810) and a blunt edge needle

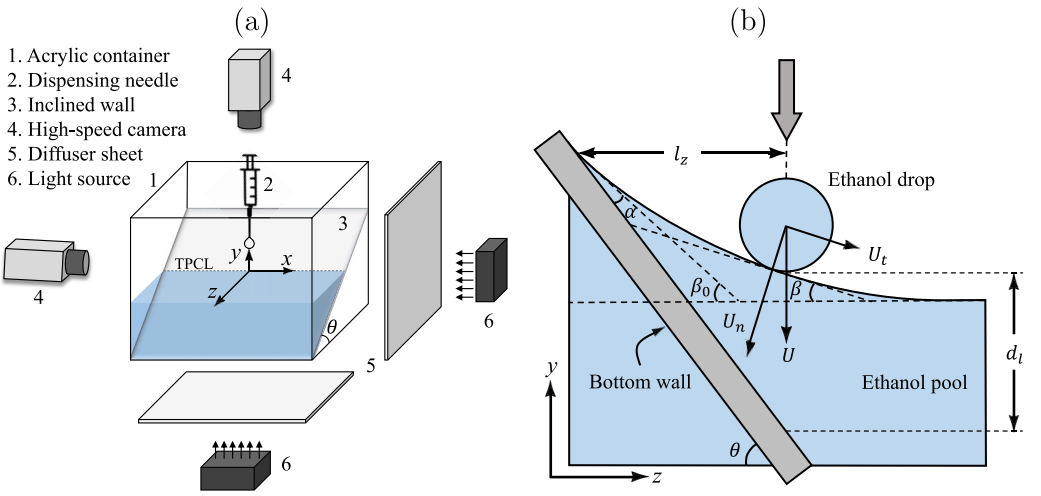

FIG. 1. (a) Schematic diagram of the experimental setup. The size of the acrylic container is 10 cm × 10 cm × 10 cm with its bottom wall inclined at an angle, θ. The thickness of the acrylic sheet is 4 mm. (b) Schematic diagram illustrating a droplet impacting with velocity (U) on the curved free surface of the ethanol pool near the TPCL. The tangential and normal components of U are $U_t = U \sin\beta$ and $U_n = U \cos\beta$, respectively. Here β represents the angle between the tangent to the free surface of the ethanol pool and the horizontal, and $\beta_0 = \theta - \alpha$ (from geometry).

(18-gauge length) with traversing mechanisms to anchor its movement in the y and z directions. The droplet generation system produces the same size of ethanol droplets of diameter, $D = 1.96$ mm, by maintaining a volumetric flow rate of 15 μl/s in the syringe pump. The depth (d_l) of the liquid at the impingement location of the droplet is calculated by measuring the horizontal distance of the needle from the TPCL (l_z) as $d_l = l_z \tan\theta$, where θ is the inclination angle of the bottom wall. The inclination angle is varied by changing the triangular bottom block (made of acrylic) in the container.

For high-speed visualization, two high-speed cameras (Phantom VEO 640L) with Rokinon lens AF 135 mm F2.0 are used in an orthogonal configuration to capture the front (y-z) and top (x-z) views of the coalescence dynamics. The front view camera's angle with the horizontal is maintained at 7° to capture the complete coalescence dynamics, and the top camera is positioned 7° off the vertical to capture the top view without the needle. We have used extension tubes with lenses to get better spatial resolution. Each camera is accompanied by a diffuser sheet and a diffused GSVITEC light source (MultiLED QT, GSVITEC, Germany). The images captured using high-speed cameras have a resolution of 1024 × 384 pixels and a spatial resolution of 19.28 μm/pixel. The images were recorded at 5000 frames per second (fps) and with an exposure time of 50 μs for all of the experiments. Both cameras are synced with a LaserPulse synchronizer (610036, TSI, USA), connected to a computer, and controlled by Phantom Camera Control (PCC 3.3) software. While the images captured from the side camera are used to calculate the migration distance and the coalescence phenomenon, the top view is utilized to eliminate scenarios where the satellite droplet deviates from its intended path (off-center movement). It also assists in the verification of the migration distance.

For experiments, the TPCL on the inclined bottom wall was carefully identified, and the dispensing needle was positioned 1 mm away from the TPCL in the z direction toward the liquid side. As the droplet diameter (D) is fixed at 1.96 mm, we selected this location as the starting point for the traversal mechanism. We have chosen a minimum dispensing height for which the droplet entirely detaches from the needle before it comes into contact with the air-liquid interface. We moved the

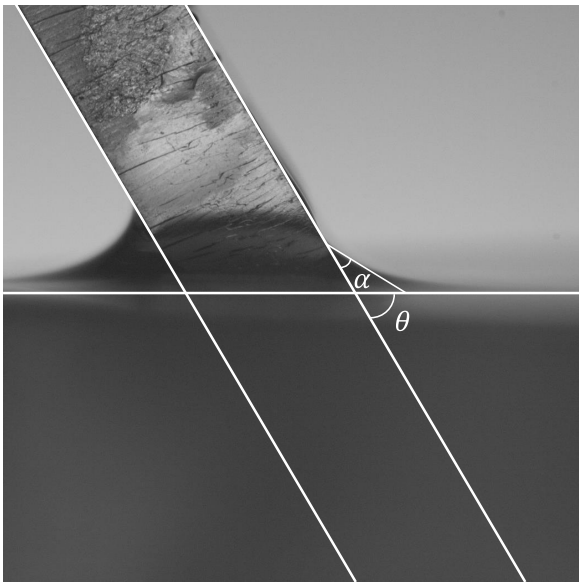

FIG. 2. A typical picture from our experiments showing the inclination angle, θ, of the bottom wall and the curvature of the ethanol-air interface near the TPCL; α represents the contact angle.

dispensing needle in the z direction from the starting position and recorded the images for every 1 mm movement of the dispensing needle, which alters the depth of the liquid in the pool while keeping the plate angle and height constant. The liquid depth in the pool was then fixed, and the height of the dispensing needle was increased by moving the dispensing needle in the y direction. The inclination angle of the bottom wall (θ) is varied as 11°, 18°, 29°, 44°, and 56° with a ±1° error in computing the angle. The density (ρ_l), dynamic viscosity (μ_l), and surface tension (σ) of ethanol are 785.8 kg/m^3, 1.1 mPa s, and 22.1 mN/m, respectively. For each set of parameters, we perform three repetitions and then calculate the error bars. It is to be noted that the run time of each experiment is less than 300 ms. Thus the effect of the evaporation on the meniscus can be neglected.

Our experiments reveal that due to the curvature of the air-liquid interface near the TPCL, the droplet migrates over the free surface of the liquid pool in the z direction while exhibiting partial coalescence and cascading of satellite droplets (decrease in size). The two high-speed imaging systems clearly capture the droplet's motion, and the results are discussed in the next section.

III. RESULTS AND DISCUSSION

Figure 2 illustrates that the formation of a concave curvature in the air-liquid interface near the TPCL on the inclined bottom wall of the ethanol-filled container plays an important role in the coalescence and migration phenomena observed in our study. The contact angle (α) formed by the air-liquid interface near TPCL increases as the bottom wall's inclination angle (θ) increases. This change in the apparent contact angle can be dedicated to the contact angle hysteresis resulting from the roughness of the surface. In the present study, we manipulate the wall's inclination to change the meniscus's inclination, causing the contact angle α to vary between 9° and 28°. However, future investigation is required to comprehend this effect better. The impact velocity of the droplet and its components when it touches the free surface of the ethanol pool near the TPCL is schematically shown in Fig. 1(b). Here β represents the angle between the tangent to the free surface of the ethanol pool and the horizontal, such that $U_t = U \sin\beta$ and $U_n = U \cos\beta$ are the tangential and normal components of the droplet's velocity at the curved air-liquid interface. Using the Young-Laplace

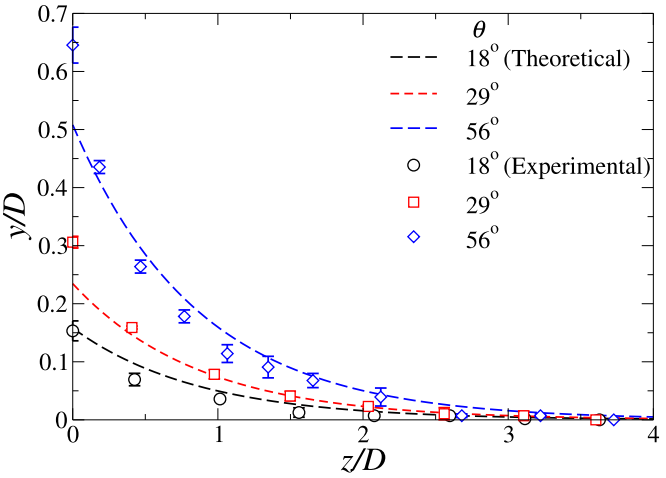

FIG. 3. Demonstration that our experimental meniscus profiles (symbols) follow the exponential decay predicted by the Young-Laplace law (dashed line) in the limit of small slope for different values of the inclination angle, θ.

equation, the shape of the meniscus can be obtained as

$$y = l_c \tan(\beta_0) e^{-z/l_c}, \tag{1}$$

where $l_c = \sqrt{\sigma/\rho_l g}$ is the capillary length and $\beta_0 = \theta - \alpha$. For ethanol, $l_c = 1.7$ mm. In the limiting cases, for $\theta = 0^\circ$ and 90°, from Eq. (1), we recover the situations associated with flat substrate and infinite liquid pool, respectively. Although this is a well-known result, the derivation of this equation is given in the Appendix for completeness. Figure 3 depicts the comparison of the meniscus obtained using Eq. (1) and that from our experiments for different values of θ. It can be seen that our experimental results follow the exponential decay predicted by the Young-Laplace law in the limit of small slope.

As the droplet impacts the free surface in the shallow depth region near the TPCL, it creates an asymmetrical depression that pulls back the droplet in the direction normal to the tangent at the free surface, while the droplet simultaneously experiences a momentum due to U_t contributing to its migration in the z direction. Subsequently, the moving droplet on the free surface exhibits partial coalescence (formation of satellite droplets) due to the upward-moving capillary waves, which are asymmetrical at first but become symmetrical as the droplet migrates in the z direction toward the deeper region in the liquid pool.

The coalescence dynamics in our study is caused by the competition between the momentum provided by the components of the droplet's impact velocity. Thus, to demonstrate the distinct behaviors, we vary the Weber number by changing the impact velocity, U, while keeping the ethanol pool's inclination angle and initial depth fixed at $\theta = 18^\circ$ and $d_l/D = 0.83$. Figures 4(a)–4(d) present the temporal evolution of the coalescence dynamics of an ethanol droplet for We = 0.32, 4.80, 7.95, and 14.27, respectively. In our study, $\tau = 0$ represents the instant when the primary droplets comes in apparent contact with the pool interface. For low Weber number (We = 0.32), the droplet floats on the free surface due to the air cushion between the droplet and the free surface of the pool while slowly migrating in the z direction (see $\tau = 1.35$). The sandwiched air is then pushed out, allowing the primary droplet to drain into the pool. Subsequently, a liquid column is generated due to upward-moving capillary waves, which is necked due to competition between the vertical and horizontal collapse rates of the liquid column, and eventually, a satellite droplet is ejected (see $\tau = 4.11$). This satellite droplet continues to migrate in the z direction while undergoing a coalescence cascade (decreasing the size of satellite droplets) with successive partial coalescence

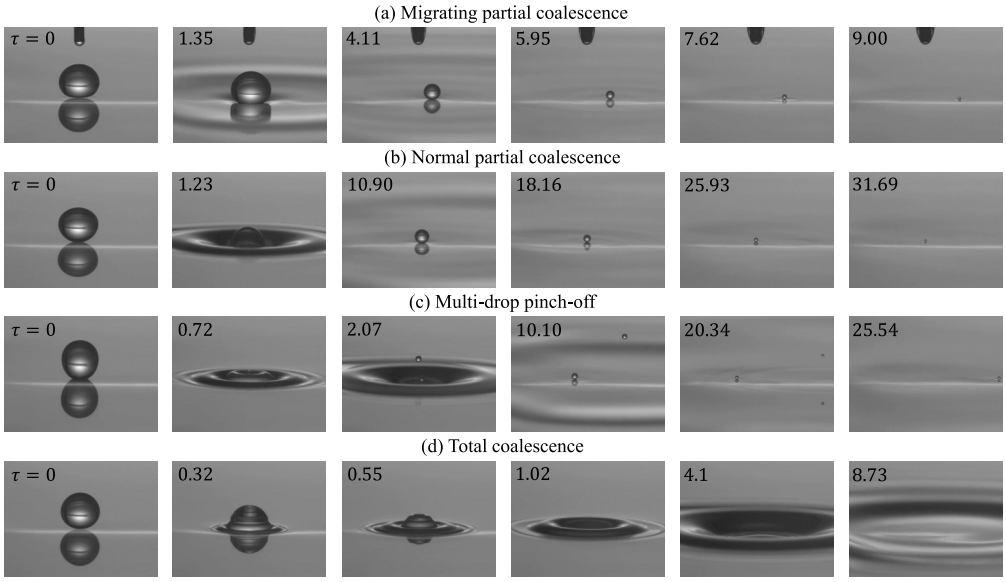

FIG. 4. Temporal evolution of the coalescence dynamics of an ethanol droplet exhibiting distinct behaviors: (a) migrating partial coalescence (We = 0.32), (b) normal partial coalescence (We = 4.80), (c) multidrop pinch-off (We = 7.95), and (d) total coalescence (We = 14.27). The dimensionless time, $\tau = tU/D$, is given at the top-left corner of each panel, such that $\tau = 0$ represents the instant when the primary droplets comes in apparent contact with the pool interface. In all cases, $\theta = 18^\circ$ and $d_l/D = 0.83$.

dynamics until the last satellite droplet merges in the ethanol pool [Fig. 4(a)]. This case is termed the migrating partial coalescence.

As the impact velocity of the droplet is increased [We = 4.80; Fig. 4(b)], the potential energy of the primary droplet counteracts the curvature effect and suppresses the movement of the droplet in the z direction. Thus, resulting in a cascading phenomenon of the satellite droplets at nearly the same impact location. It can also be seen that the primary droplet forms a bigger crater (see $\tau = 1.23$) on the free surface as compared to that for We = 0.32. This case is similar to the normal partial coalescence dynamics observed in orthogonal impacts.

Due to moderately high impact velocity for We = 7.95, the primary droplet penetrates the pool and quickly reaches the inclined bottom wall and, thus, bounces back in an upward direction [Fig. 4(c)]. In this case, two or more satellite droplets are formed due to the interplay of the capillary forces and vertical collapse of the primary droplet ($\tau = 2.07$). These satellite droplets come down again to the free surface, and cascading occurs until they fully merge inside the pool. This condition is referred to as a multidrop pinch-off. For high Weber number (We = 14.27), the droplet exhibits complete coalescence [Fig. 4(d)]. Close inspection of Fig. 4 reveals that the residence time, which is defined as the time elapsed between the instants when the droplet touches the air-liquid interface (first column) and the onset of the coalescence (second column), decreases with increasing the Weber number. The air cushion between the droplet and the free surface drains quickly as the Weber number increases, reducing the droplet's residence time.

To gain more insight, we compare the temporal evolution of the droplet profiles during the coalescence process in Figs. 5(a)–5(d) for four different sets of parameters: ($\theta = 18^\circ$, We = 1.98, $d_l/D = 1.16$), ($\theta = 18^\circ$, We = 0.32, $d_l/D = 0.17$), ($\theta = 18^\circ$, We = 1.98, $d_l/D = 0.17$), and ($\theta = 56^\circ$, We = 0.32, $d_l/D = 0.76$), respectively. At $\tau = 0$ (which corresponds to the dimensionless migration distance, $L_z/D = 0$), it can be seen that the droplet is spherical, and it undergoes vertical oscillations at the early stage owing to the pushing out and regaining the thin air cushion between the

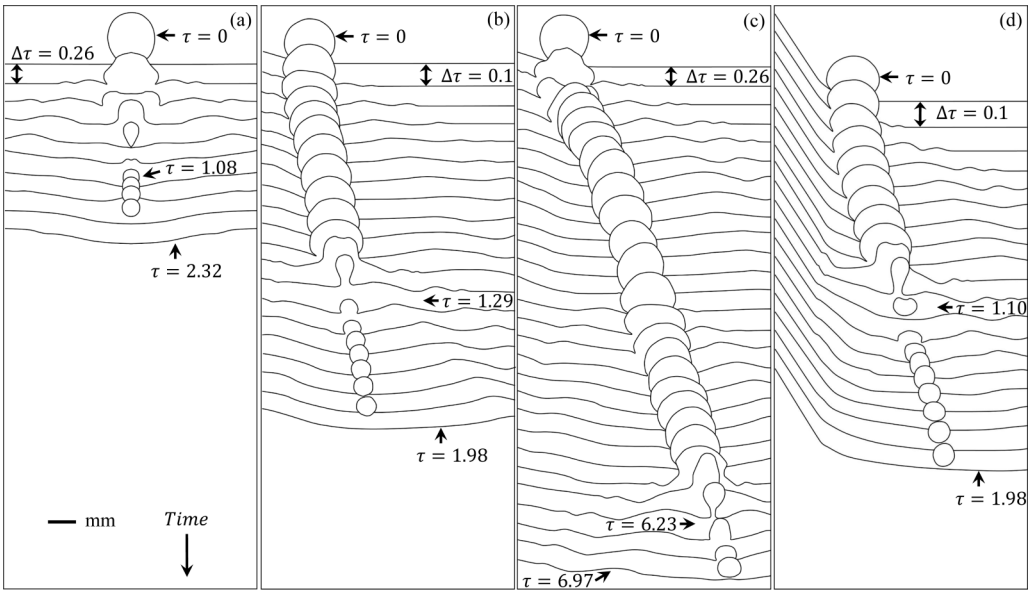

FIG. 5. Temporal evolution of the air-liquid interface and the droplet profile for (a) $\theta = 18°$, We $= 1.98$, $d_l/D = 1.16$; (b) $\theta = 18°$, We $= 0.32$, $d_l/D = 0.17$; (c) $\theta = 18°$, We $= 1.98$, $d_l/D = 0.17$; and (d) $\theta = 56°$, We $= 0.32$, $d_l/D = 0.76$. The time interval, $\Delta\tau$, between two constitutive profiles used for each set of parameters is given in each panel. The animations corresponding to panels (a)–(d) are provided as supplemental videos 1–4 [41], respectively.

droplet and the free surface. These early oscillations are more pronounced for high Weber number. Then the droplet drains inside the pool resulting in capillary waves on the air-liquid interface. In Fig. 5(a) the values of θ and We are the same, but the depth of the liquid pool is higher than that as in Fig. 5(c). In this case, due to the flat free surface at the location of primary impact, the coalescence dynamics occurs mostly at the location of primary impact, and the satellite droplets do not exhibit any lateral migration. In Fig. 5(b), due to the momentum gaining from the curvature, the primary droplet, while undergoing coalescence, migrates in the z direction and travels a distance $L_z/D = 0.75$, where it exhibits partial coalescence and pinches off the first satellite droplet at $\tau = 1.29$. The first satellite droplet also continues to migrate and undergoes subsequent partial coalescences (cascading). Here we have shown till $\tau = 1.98$ when the first satellite droplet travels a distance $L_z/D = 1.14$.

Figure 5(c) is for We $= 1.98$ with the rest of the parameters the same as in Fig. 5(b). As shown in Fig. 1(b), increasing We increases the tangential component of the impact velocity, U_t, which in turn increases the total migration of the droplet in the z direction away from the TPCL. At the onset of the first partial coalescence, at $\tau = 6.97$, the primary droplet has migrated a distance of $L_z/D = 3.31$. The parameters considered in Fig. 5(d) are $\theta = 56°$, We $= 0.32$, and $d_l/D = 0.76$. For $\theta = 56°$, the tangential component of the impact velocity of the droplet is significantly higher than the normal component. This suppresses the vertical oscillations but increases the migration speed and distance traveled by the droplet. In this case, till the onset of the first partial coalescence at $\tau = 1.10$, the droplet has already traveled a distance $L_z/D = 0.99$. The satellite droplet also migrates faster and travels a distance $L_z/D = 1.81$ at $\tau = 1.98$. Close inspection of Fig. 5(d) also reveals that due to the dominance of U_t over U_n, the satellite droplet continues to float on the free surface for a long time while migrating in the z direction. The total migration distance in Fig. 5(d) is about three times greater than that in Fig. 5(b). Thus, we can conclude that the curvature of the air-liquid interface

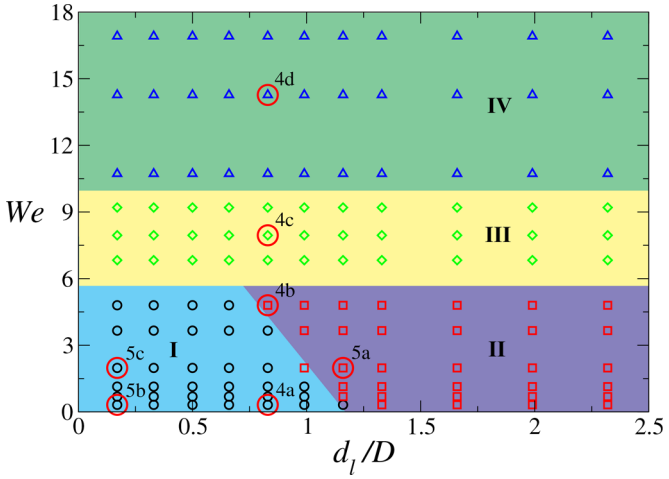

FIG. 6. Regime map demarcating different coalescence phenomena: the migrating partial coalescence (I), normal partial coalescence (II), multidrop pinch-off (III), and total coalescence (IV) in d_l/D-We space for $\theta = 18^\circ$. The red circles show the data points considered in Figs. 4 and 5.

near TPCL resulting from the inclination of the bottom wall is important for the migration of the droplet over the free surface of the liquid pool.

It was established in Fig. 4 that by varying the Weber number, we get distinct coalescence behaviors. The depth of the liquid pool, which increases as we move the dispensing needle away from the TPCL, is another factor that influences coalescence dynamics. Thus, in Fig. 6, we plot the regime map that demarcates different coalescence behaviors of the droplet in d_l/D-We space. For low We (when the droplet is placed on the free surface gently), the droplet encounters the curvature effect and therefore undergoes migration when impacted in the shallow liquid depth (low d_l/D) region (region I). In contrast, when d_l/D is high, the droplet undergoes a normal partial coalescence behavior (region II). As the Weber number is increased from low to moderate values, the coalescence mode changes from the migrating partial coalescence and normal partial coalescence to the multidrop pinch-off (region III), regardless of the liquid depth (d_l/D). It is to be noted that the multidrop pinch-off occurs when inertia force overcomes the surface tension force. The droplet penetrates and touches the lower part of the pool when impacted with a higher impact velocity. Thus, the bottom part of the droplet comes to rest while its upper part is still in motion, which creates a dimple on the summit of the droplet [see at $\tau = 0.72$ in Fig. 4(c)]. Subsequently, a thin liquid column is formed due to the upward-moving capillary waves, and a tiny satellite droplet pinches off due to the partial coalescence process. Both the droplet and the pool liquid move down at this stage while the column structure occurs upward. This results in the Plateau-Rayleigh instability on the column surface while it elongates. Due to this, more satellite droplets are formed [see at $\tau = 2.07$ in Fig. 4(c)]. In region IV the inertia of the droplet is most dominant, and, thus, the primary droplet undergoes a complete coalescence process. As the multidrop pinch-off and total coalescence are mostly surface phenomena, the depth of the liquid pool has no effect on them. The upper boundary of region III (We $\approx$ 10) represents the transition of the partial coalescence to the complete coalescence (region IV). A similar value of the transitional Weber number was also reported by Leneweit *et al.* [28]. For a droplet impacting on another droplet, Abouelsoud and Bai [40] observed the complete coalescence behavior for We $>$ 8. For a droplet impacting on a thin film, Pan and Law [42] found that a droplet undergoes the transition from bouncing to complete coalescence behavior for We $\approx$ 14.

The following discussion highlights the similarity and differences between the coalescence behavior observed in the present study with the earlier investigations involving oblique impacts

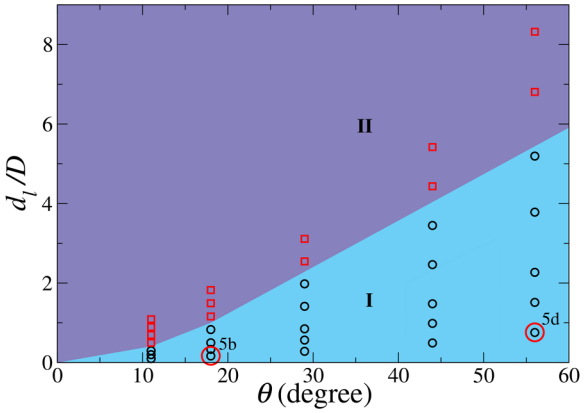

FIG. 7. Regime map showing the migrating partial coalescence (I) and normal partial coalescence (II) in θ-d_l/D space for We = 0.32. The red circles show the data points considered in Fig. 5.

and moving films. Alghoul *et al.* [30] investigated the impact dynamics of a droplet on a horizontal moving film. They observed that for We = 0.6, the droplet floats on the free surface for about 1 s on a moving film of depth $d_l/D = 1.74$ and undergoes migrated partial coalescence dynamics for We = 4.5. Although this behavior is consistent with our regime map (Fig. 6), the floating time of the droplet in our study is about 38.8 ms. The longer floating time observed in the study of Alghoul *et al.* [30] is due to the moving film, which replenishes the air cushion between the droplet and the liquid film that helps the droplet to float. Alghoul *et al.* [30] also found complete coalescence for We = 41. Although in our regime map (Fig. 6), we presented up to We = 18, the behavior of complete coalescence observed by Alghoul *et al.* [30] lies in our region IV (as we observe the total coalescence for We > 10). Like in the present study, they also observed that the region of complete coalescence is independent of their film thickness. For a droplet impacting on a 45° inclined liquid film, Che *et al.* [27] observed that the transition from bouncing/partial coalescence to total coalescence happens at We ≈ 20. In another study, by varying the height of a horizontal liquid pool, Tang *et al.* [43] found that a droplet undergoes the transition from bouncing to complete coalescence at We ≈ 15. Our finding of the total coalescence for We > 10 also agrees with the result of Liu [14] who investigated the impact of a droplet on a horizontal film with the surrounding air moving at a fixed velocity. Okawa *et al.* [26] investigated the effect of the impingement angle of a droplet on a horizontal liquid pool and found that the deposition-splashing boundary depends on the absolute velocity of the impacting droplet and not just the normal component of the velocity. The splashing-deposition limit was found to be independent of both the impact angle of primary drop and the dimensionless thickness of the pool depth. This is similar to the present study as we also observe the transition between regions exhibiting partial coalescence (I and II) and multidrop pinch-off (III) and the transition between regions III and IV (complete coalescence) for different depths of the pool occur at fixed values of the Weber numbers (independent of d_l/D).

Figure 7 depicting the migrating partial coalescence (I) and normal partial coalescence (II) regions in the θ-d_l/D space again highlights the effect of curvature formed by the air-liquid interface near the TPCL on the coalescence dynamics. As discussed above, the increasing inclination angle (θ) of the bottom wall increases the contact angle (α) at the TPCL due to the contact angle hysteresis, which in turn increases β (the angle between the tangent to the free surface of the ethanol pool and the horizontal). Thus, for a fixed liquid depth at the location of droplet impingement (d_l/D), increasing θ changes the normal partial coalescence to migrating partial coalescence. Similarly, for a fixed θ value, increasing the liquid depth decreases the influence of β, which becomes negligible after a certain value of d_l/D. Therefore, the mode of coalescence changes from the migrating to normal partial coalescence as we increase d_l/D for a fixed value of θ.

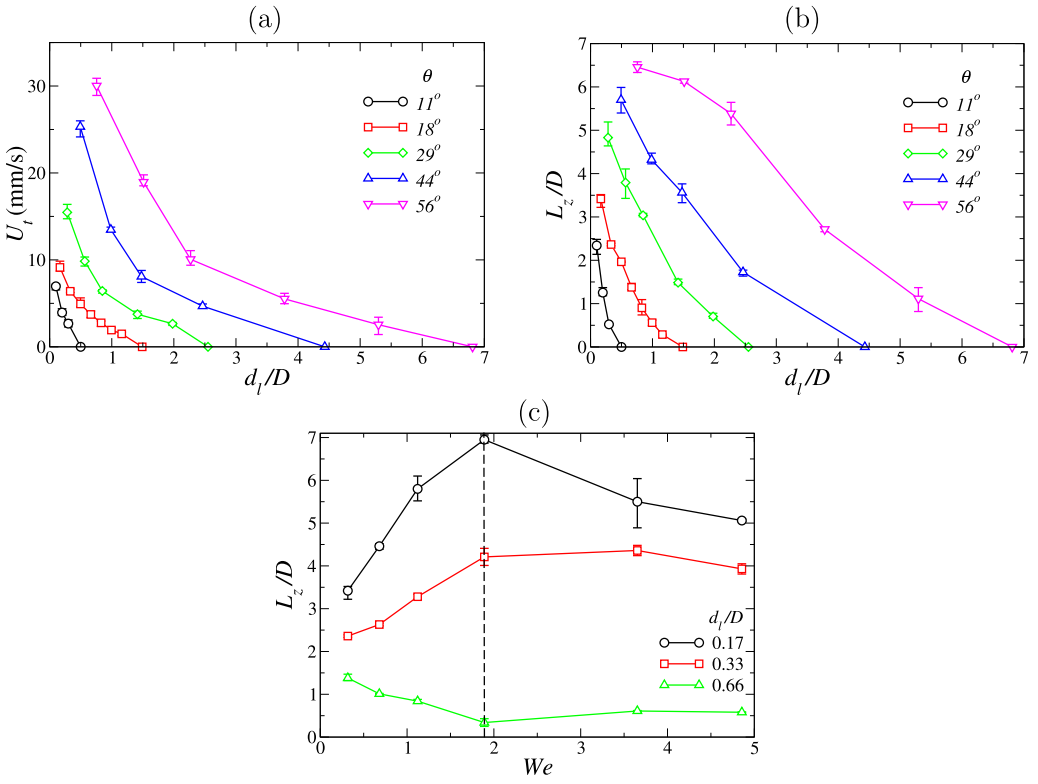

FIG. 8. Variations of (a) the tangential velocity, $U_t = U \sin\beta$, and (b) the total migrated distance (L_z/D) with the depth of the ethanol pool (d_l/D) for different values of the inclination angle, θ, for We $= 0.32$. (c) Variations of L_z/D with We for different values d_l/D at $\theta = 18^\circ$.

The dependency of the tangential velocity (U_t) and total migration distance (L_z/D) of the droplet with the depth of the liquid pool at the point of impact (d_l/D), inclination angle (θ), and Weber number We are summarized in Figs. 8(a)–8(c), which quantify the findings discussed above. Figures 8(a) and 8(b) also depict the values of d_l/D at which U_t and L_z/D reach zero, thereby indicating the transition from migrated to normal partial coalescence. Moreover, it can be seen in Fig. 8(c) that for $\theta = 18^\circ$ a clear transition occurs at We ≈ 2, after which the inclined wall influences the coalescence dynamics. This value of the critical Weber number increases with increasing the inclination angle. It can be seen in Fig. 8(c) that, for shallow depths ($d_l/D = 0.17$ and 0.33), increasing the dispensing height of the needle (i.e., increasing We) increases the impact velocity and hence increases the tangential velocity component of the droplet, resulting in higher migration. After the critical value (We ≈ 2), the impact of the droplet is sufficient to form a depression on the interface, which is extended to the plate. As a result, once the droplet makes contact with the inclined plate. This dissipates some energy, and thus the migration of the droplet decreases for higher values of We. In contrast, for $d_l/D = 0.66$, the depression created due to the impact is insufficient to reach the inclined surface, and thus, we observe a negligible effect of the plate in this case. Moreover, for $d_l/D = 0.66$, $\beta = 3.8^\circ$. This is very small, resulting in small tangential velocity and thus less migration. Lo *et al.* [44] observed two distinct migration speeds when a droplet comes in contact with a smooth surface during its residence period and after it touches the surface. We found that the total time of coalescence in all the cases (for different Weber numbers and dispensing heights) considered in our study is about $t = 273 \pm 27$ ms. It is to be noted that the residence time of the satellite droplet is arbitrary. However, the total distance traveled by the droplet depends on the

Weber number and the curvature of the free surface. We also observed that the residence time of the primary droplet varies randomly (albeit very small) with the change in the Weber number and inclination angle. Thus, there is no direct relationship between the total coalescence time and the distance traveled by the droplets.

IV. CONCLUDING REMARKS

We investigate the coalescence dynamics of an ethanol droplet impacting vertically on an ethanol pool with an inclined bottom wall using a high-speed shadowgraph technique. We observe some unique coalescence phenomena, such as migrating partial coalescence and multidrop pinch-off dynamics by varying the Weber number (We), the liquid depth at the point of impact (d_l/D), and inclination angle (θ). Our experiments reveal that the three-phase contact line (TPCL) created by the air-liquid interface on the inclined bottom wall and its curvature near the TPCL are the mechanisms underlying these coalescence behaviors. The competition between the tangential and normal components of the droplet's impact velocity at the curved air-liquid interface near the TPCL causes the distinct coalescence behaviors observed in our study. For high We, the droplet undergoes complete coalescence. The regime maps plotted in d_l/D-We and θ-d_l/D spaces clearly demarcate the different coalescence behaviors. We find that the transition between the partial coalescence and complete coalescence occurs at We ≈ 10, which is independent of the liquid depth and is consistent with the finding reported by Leneweit *et al.* [28]. Moreover, it is observed that for $\theta = 18^\circ$, the effect of the inclined wall is significant for We > 2; this critical value of We increases with increasing the inclination angle.

ACKNOWLEDGMENTS

K.C.S. thanks the Science & Engineering Research Board, India for their financial support (Grant No. CRG/2020/000507). We are thankful to the anonymous reviewers and an associate editor for their constructive suggestions, which help us to improve the manuscript significantly. The authors report no conflict of interest.

APPENDIX: MENISCUS SHAPE OBTAINED USING THE YOUNG-LAPLACE EQUATION

Applying the Young-Laplace equation at the free surface, $y = f(z)$, gives

$$\rho_l g y - \frac{\sigma}{R} = \text{const}, \tag{A1}$$

where y is the height of the meniscus, ρ_l is the density of liquid, σ is surface tension, g is the acceleration due to gravity, and R is the radius of curvature of the free surface, such that $1/R = \nabla \cdot n$. Here n is the outward pointing normal to the free surface. Thus, it can be shown that

$$\frac{1}{R} = \frac{y''}{(y'^2 + 1)^{3/2}}, \tag{A2}$$

where the prime represents the derivative of y with respect to z. Substituting this expression in Eq. (A1), we obtain

$$\rho_l g y - \frac{\sigma y''}{(y'^2 + 1)^{3/2}} = \text{const}. \tag{A3}$$

As far from the wall, the interface is flat, the constant becomes zero, and the resultant equation becomes

$$y'' = \frac{\rho_l g y}{\sigma}(1 + y'^2)^{3/2}. \tag{A4}$$

For $y' \ll 1$ (i.e., for thin inclined surfaces), we get

$$y'' = \frac{y}{{l_c}^2}, \tag{A5}$$

where $l_c = \sqrt{\sigma/\rho_l g}$ is the capillary length. We can obtain the meniscus profile, $y(z)$, by solving Eq. (A5) using the following boundary conditions [45]:

$$dy/dz = -\tan\beta_0 \quad \text{at } z = 0 \quad \text{and} \tag{A6}$$

$$y = 0 \quad \text{at } z \to \infty. \tag{A7}$$

where $\beta_0 = \theta - \alpha$. Thus, the final expression of the meniscus profile is given by

$$y = l_c \tan(\beta_0) e^{-z/l_c}. \tag{A8}$$

For ethanol, $l_c = 1.7$ mm.

[1] G. S. Chaitanya, K. C. Sahu, and G. Biswas, A study of two unequal-sized droplets undergoing oblique collision, Phys. Fluids **33**, 022110 (2021).

[2] M. K. Tripathi, A. R. Premlata, K. C. Sahu, and R. Govindarajan, Two initially spherical bubbles rising in quiescent liquid, Phys. Rev. Fluids **2**, 073601 (2017).

[3] D. Legendre, J. Magnaudet, and G. Mougin, Hydrodynamic interactions between two spherical bubbles rising side by side in a viscous liquid, J. Fluid Mech. **497**, 133 (2003).

[4] F. H. Zhang, E. Q. Li, and S. T. Thoroddsen, Satellite Formation during Coalescence of Unequal Size Drops, Phys. Rev. Lett. **102**, 104502 (2009).

[5] T. Gilet and J. W. M. Bush, Droplets bouncing on a wet, inclined surface, Phys. Fluids **24**, 122103 (2012).

[6] X. Yang, V. H. Chhasatia, J. Shah, and Y. Sun, Coalescence, evaporation and particle deposition of consecutively printed colloidal drops, Soft Matter **8**, 9205 (2012).

[7] Š. Šikalo, C. Tropea, and E. N. Ganić, Impact of droplets onto inclined surfaces, J. Colloid Interface Sci. **286**, 661 (2005).

[8] H. A. Stone, A. D. Stroock, and A. Ajdari, Engineering flows in small devices: Microfluidics toward a lab-on-a-chip, Annu. Rev. Fluid Mech. **36**, 381 (2004).

[9] S. T. Thoroddsen, T. G. Etoh, and K. Takehara, High-speed imaging of drops and bubbles, Annu. Rev. Fluid Mech. **40**, 257 (2008).

[10] M. Kumar, R. Bhardwaj, and K. C. Sahu, Coalescence dynamics of a droplet on a sessile droplet, Phys. Fluids **32**, 012104 (2020).

[11] T. B. Low and R. List, Collision, coalescence and breakup of raindrops. Part I: Experimentally established coalescence efficiencies and fragment size distributions in breakup, J. Atmos. Sci. **39**, 1591 (1982).

[12] J. J. Thomson and H. F. Newall, On the formation of vortex rings by drops falling into liquids, and some allied phenomena, Proc. R. Soc. Lond. **39**, 417 (1886).

[13] H. C. Pumphrey, L. A. Crum, and L. Bjørnø, Underwater sound produced by individual drop impacts and rainfall, J. Acoust. Soc. Am. **85**, 1518 (1989).

[14] X. Liu, Experimental study of drop impact on deep-water surface in the presence of wind, J. Phys. Oceanogr. **48**, 329 (2018).

[15] S. T. Thoroddsen and K. Takehara, The coalescence cascade of a drop, Phys. Fluids **12**, 1265 (2000).

[16] X. Chen, S. Mandre, and J. J. Feng, Partial coalescence between a drop and a liquid-liquid interface, Phys. Fluids **18**, 051705 (2006).

[17] T. Gilet, K. Mulleners, J. P. Lecomte, N. Vandewalle, and S. Dorbolo, Critical parameters for the partial coalescence of a droplet, Phys. Rev. E **75**, 036303 (2007).

[18] B. Ray, G. Biswas, and A. Sharma, Generation of secondary droplets in coalescence of a drop at a liquid–liquid interface, J. Fluid Mech. **655**, 72 (2010).

[19] F. H. Zhang, M. J. Thoraval, S. T. Thoroddsen, and P. Taborek, Partial coalescence from bubbles to drops, J. Fluid Mech. **782**, 209 (2015).
[20] H. Deka, G. Biswas, K. C. Sahu, Y. Kulkarni, and A. Dalal, Coalescence dynamics of a compound drop on a deep liquid pool, J. Fluid Mech. **866**, R2 (2019).
[21] P. K. Kirar, K. Alvarenga, P. Kolhe, G. Biswas, and K. C. Sahu, Coalescence of drops on the free-surface of a liquid pool at elevated temperatures, Phys. Fluids **32**, 052103 (2020).
[22] F. Blanchette and T. P. Bigioni, Dynamics of drop coalescence at fluid interfaces, J. Fluid Mech. **620**, 333 (2009).
[23] O. W. Jayaratne and B. J. Mason, The coalescence and bouncing of water drops at an air/water interface, Proc. R. Soc. Lond. A **280**, 545 (1964).
[24] M. V. Gielen, P. Sleutel, J. Benschop, M. Riepen, V. Voronina, C. W. Visser, D. Lohse, J. H. Snoeijer, M. Versluis, and H. Gelderblom, Oblique drop impact onto a deep liquid pool, Phys. Rev. Fluids **2**, 083602 (2017).
[25] B. Ray, G. Biswas, and A. Sharma, Oblique drop impact on deep and shallow liquid, Commun. Comput. Phys. **11**, 1386 (2012).
[26] T. Okawa, T. Shiraishi, and T. Mori, Effect of impingement angle on the outcome of single water drop impact onto a plane water surface, Exp. Fluids **44**, 331 (2008).
[27] Z. Che, A. Deygas, and O. K. Matar, Impact of droplets on inclined flowing liquid films, Phys. Rev. E **92**, 023032 (2015).
[28] G. Leneweit, R. Koehler, K. G. Roesner, and G. Schäfer, Regimes of drop morphology in oblique impact on deep fluids, J. Fluid Mech. **543**, 303 (2005).
[29] F. Blanchette and T. P. Bigioni, Partial coalescence of drops at liquid interfaces, Nat. Phys. **2**, 254 (2006).
[30] S. K. Alghoul, C. N. Eastwick, and D. B. Hann, Normal droplet impact on horizontal moving films: An investigation of impact behaviour and regimes, Exp. Fluids **50**, 1305 (2011).
[31] G. E. Cossali, A. Coghe, and M. Marengo, The impact of a single drop on a wetted solid surface, Exp. Fluids **22**, 463 (1997).
[32] A. B. Wang and C. C. Chen, Splashing impact of a single drop onto very thin liquid films, Phys. Fluids **12**, 2155 (2000).
[33] B. Gopalan and J. Katz, Turbulent Shearing of Crude Oil Mixed with Dispersants Generates Long Microthreads and Microdroplets, Phys. Rev. Lett. **104**, 054501 (2010).
[34] E. Castillo-Orozco, A. Davanlou, P. K. Choudhury, and R. Kumar, Droplet impact on deep liquid pools: Rayleigh jet to formation of secondary droplets, Phys. Rev. E **92**, 053022 (2015).
[35] X. Gao and R. Li, Impact of a single drop on a flowing liquid film, Phys. Rev. E **92**, 053005 (2015).
[36] J. R. Castrejón-Pita, B. N. Muñoz-Sánchez, I. M. Hutchings, and A. A. Castrejón-Pita, Droplet impact onto moving liquids, J. Fluid Mech. **809**, 716 (2016).
[37] D. A. Burzynski and S. E. Bansmer, Droplet splashing on thin moving films at high Weber numbers, Int. J. Multiphase Flow **101**, 202 (2018).
[38] J. C. Bird, S. S. H. Tsai, and H. A. Stone, Inclined to splash: Triggering and inhibiting a splash with tangential velocity, New J. Phys. **11**, 063017 (2009).
[39] F. Blanchette, L. Messio, and J. W. M. Bush, The influence of surface tension gradients on drop coalescence, Phys. Fluids **21**, 072107 (2009).
[40] M. Abouelsoud and B. Bai, Bouncing and coalescence dynamics during the impact of a falling drop with a sessile drop on different solid surfaces, Phys. Fluids **33**, 063309 (2021).
[41] See Supplemental Material at http://link.aps.org/supplemental/10.1103/PhysRevFluids.7.094001 for animations showing the distinct dynamics of a droplet on a liquid pool with an inclined bottom wall.
[42] K. L. Pan and C. K. Law, Dynamics of droplet–film collision, J. Fluid Mech. **587**, 1 (2007).
[43] X. Tang, A. Saha, C. K. Law, and C. Sun, Bouncing-to-merging transition in drop impact on liquid film: Role of liquid viscosity, Langmuir **34**, 2654 (2018).
[44] H. Y. Lo, Y. Liu, and L. Xu, Mechanism of Contact between a Droplet and an Atomically Smooth Substrate, Phys. Rev. X **7**, 021036 (2017).
[45] A. Mishra, V. Kulkarni, J. W. Khor, and S. Wereley, Mapping surface tension induced menisci with application to tensiometry and refractometry, Soft Matter **11**, 5619 (2015).